Variable Powder Flow Rate Control in Laser Metal Deposition Processes

Lie Tang, Jianzhong Ruan, Robert G. Landers, and Frank Liou

University of Missouri–Rolla

Department of Mechanical and Aerospace Engineering

1870 Miner Circle, Rolla, Missouri 65409–0050

{ltx8d;jzruan;landersr;liou}@umr.edu

Reviewed, accepted August 21, 2007

Abstract

This paper proposes a novel technique, called Variable Powder Flow Rate Control (VPFRC), for the regulation of powder flow rate in laser metal deposition processes. The idea of VPFRC is to adjust the powder flow rate to maintain a uniform powder deposition per unit length even when disturbances occur (e.g., the motion system accelerates and decelerates). Dynamic models of the powder delivery system motor and the powder transport system (i.e., five–meter pipe, powder dispenser, and cladding head) are first constructed. A general tracking controller is then designed to track variable powder flow rate references. Since the powder flow rate at the nozzle exit cannot be directly measured, it is estimated using the powder transport system model. The input to this model is the DC motor rotation speed, which is estimated on–line using a Kalman filter. Experiments are conducted to examine the performance of the proposed control methodology. The experimental results demonstrate that VPFRC is successful in maintaining a uniform track morphology, even when the motion control system accelerates and decelerates.

1. Introduction

Laser Metal Deposition (LMD) is an important Solid Freeform Fabrication (SFF) technology based on three–dimensional laser cladding [1]. Similar to other processes such as Laser Engineered Net Shaping (LENS) [2], Laser–Based Additive Manufacturing (LBAM) [3], etc., LMD allows direct fabrication of functional metal parts directly from CAD solid models, as well as thin parts since the processing forces are low. It can also be used to repair parts; thus, reducing scrap and extending product service life. However, LMD processes typically utilize a constant powder flow rate and, thus, the track morphology will not remain constant when disturbances, such as motion system acceleration and deceleration, occur.

Powder flow rate control has been an issue since the inception of laser cladding technologies. The difficulty in real–time control of powder flow rate arises from the lack of sensors, or techniques, which can reliably measure, or determine, the powder flow rate during the process. Different methods have been proposed to solve the powder flow rate measurement problem. Many industrial powder feeders are equipped with a weight–loss metering system to regulate powder flow rate [4]. The powder feeder is placed on a highly sensitive scale capable of measuring small weight changes. The powder flow rate is then determined by dividing the weight change during each sample by the sample period. However, this technique is not adequate for on–line powder flow rate control due to the inherent low sampling frequency (e.g., 10 *Hz*). Another technique reported for sensing powder flow rate is the use of an optoelectronic sensor [5]. It consists of a laser diode, a photo diode, and a glass window. The laser beam emitted from the laser diode passes through the powder stream flowing inside the glass chamber and is received by the photo diode. The laser energy received by the photo diode decreases when the powder flow rate increases. Thus, the laser energy received by the photo diode can be calibrated

to powder flow rate and used as a feedback signal. The main drawback of this sensor is that it cannot be used for in–process feedback since it cannot sustain the high temperatures present at the nozzle outlet. Another powder flow rate sensing technique utilizes a compact pressure sensor [6]. It assumes that higher flow rates require higher gas pressures; therefore, powder flow rate can be calibrated to the measured gas pressure and used as a feedback signal. This sensing technique was experimentally implemented on a powder feeder using a screw feed mechanism with compressed air as the carrier gas.

In addition to developments in powder flow rate measurement, powder flow rate control design methodologies have been reported in the literature. Traditional Proportional plus Integral plus Derivative (PID) control is adopted in [6]. A more recent study [7] employs a modified PI controller. The powder flow rate is estimated through an observer using the powder feeder motor encoder signal. To account for the inherent material transport delay, the controller is implemented in a Smith Predictor Corrector Structure (SPCS). Simulation studies demonstrate good performance in controlling the powder flow rate. However, these techniques are limited in that they are only guaranteed to maintain a constant powder flow rate.

Currently, most of the reported experimental LMD studies employ a constant powder flow rate, which does not take the inherent accelerations and decelerations of motion system into consideration. Therefore, if a constant powder flow rate strategy is employed, there will be excessive powder deposited at points along the deposition path where motion system acceleration or deceleration occurs. This will result in a non–uniform track morphology. It will also cause porosity and dilution problems, which will deteriorate part quality. A better strategy is to use variable powder flow rate. The idea is to maintain a constant powder distribution along the deposition path; therefore, the powder flow rate changes when the motion system speed changes.

Variable powder flow rate control can help maintain a uniform track morphology even as the motion system accelerates and decelerates.

The rest of the paper is organized as follows. Section 2 introduces the powder delivery system mechanical and control hardware. The powder delivery system motor and powder transport system models are formulated in Section 3 and the controller methodology is presented in Section 4. In Section 5, experiments are conducted, and the results are presented and discussed. Finally, in Section 6, the paper is summarized and concluding remarks are presented.

2. System Hardware

In this section the powder delivery system mechanical and control hardware are described in detail.

2.1 Powder Delivery System

The powder delivery system (Bay State Surface Technologies model 1200) consists of a Direct Current (DC) motor and a powder transport system that includes a five–meter pipe, powder dispenser, and cladding head. The cladding head (Precitec model KG YC50) consists of a coaxial nozzle, focusing optics, and cooling system. A schematic of the powder delivery system is shown in Figure 1. The powder mass flow rate is determined by the speed of the metering wheel driven by a DC motor with a gear ratio of 102.4:1. Powder is transported to the powder dispenser by pressurized carrier gas (argon) through a hose. It is then split into four powder streams. These four streams are carried through four tubes to a coaxial nozzle, where they converge to form a cone–shaped powder stream with the same central axis as the laser beam. This powder cone finally reaches the laser–generated molten pool on the part surface.

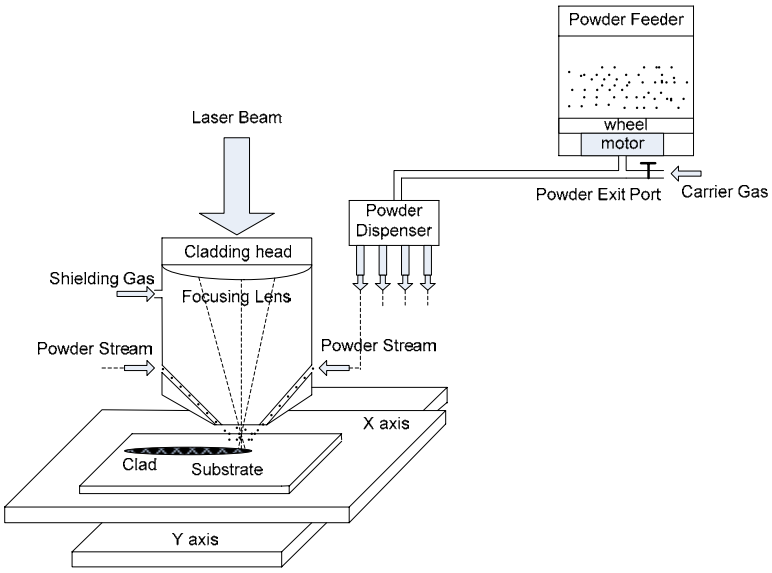

Figure 1: Powder delivery system schematic.

2.2 Powder Flow Rate Control System Hardware

The powder flow rate control system consists of a National Instruments Real Time (NI RT) control system and a PC that runs LabVIEW 8.0. Control of the powder flow rate is achieved through three boards installed on a PXI 1010 chassis: a PXI–8195 control board to run the powder flow rate data acquisition and control program, a counter/timer board (PXI 6602) to acquire digital encoder signals from the DC motor, and an analog output board (PXI 6711) to send control voltages to the DC motor amplifier. The PXI–8195 board is equipped with a 1.5*GHz* Celeron M 370 processor, a 40 gigabyte hard drive, and 2 gigabytes of DDR–2 RAM. The PXI 6602 board has 8 counters and 100 *kHz* and 20 *MHz* internal timers for counting and timing operations. The quadrature encoding mode is used for motor angular position measurement providing a resolution of $1.53 \cdot 10^{-3}$ *rad*. The PXI6711 board has 8 analog output channels, each with a range from $-10V$ to $+10V$ and 12 bits, providing a resolution of 4.88 *mV*.

The control system hardware structure is shown in Figure 2. The control program is first constructed on a PC using LabVIEW 8.0 and then downloaded to the NI RT control system via an Ethernet connection.

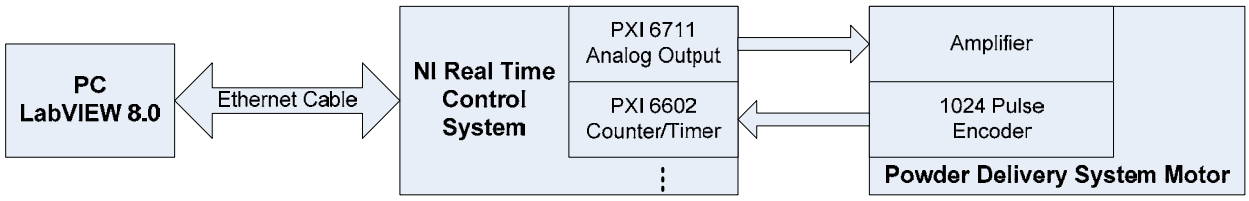

Figure 2: Powder flow rate control system hardware schematic.

3. Powder Delivery System Model

In the proposed scheme, the powder delivery system is divided into two parts, DC motor and powder transport system (i.e., five–meter pipe, powder dispenser, and cladding head), and modeled separately. In this section, these two models are constructed. Note that the powder transport system model depends on the powder material [9], which is H13 tool steel for all experiments in this paper.

3.1 DC Motor Model

The first–order DC motor model is

$$\tau_m \dot{\omega}(t) + \omega(t) = k_m V_c(t) - T_f \tag{1}$$

where τ_m is the time constant (sec), ω is the motor rotational speed (rpm), k_m is the steady–state gain (rpm/V), V_c is the command voltage (V), and T_f is the motor Coulomb friction (rpm). Note that in this form, the motor Coulomb friction is in units of rotational speed and it is a constant since the motor only operates with a positive velocity and is beyond the stictional effects. To

determine the model parameters, a series of constant command voltage signals are sent to the motor amplifier and the resulting rotational speed is measured. The model parameters are then determined by applying a Particle Swarm Optimization (PSO) algorithm [8]. The PSO algorithm is an artificial intelligence technique where a group of solutions (i.e., swarm) evolve as a function of the best solution each member of the group has obtained and the best solution the group has obtained. The resulting motor model parameters are $\tau_m = 0.121$ *sec*, $k_m = 158$ (*rpm*)/*V*, and $T_f = 98.8$ *rpm*. The comparison between the experimental data used to develop the model and the corresponding simulation data is shown in Figure 3. The results show that the DC motor model response fits the experimental data very well, especially in the low speed area. The average error percentage is

$$\overline{e} = \frac{\sum_{i=1}^{n} \left| \frac{\omega_{model}(i) - \omega_{measured}(i)}{\omega_{measured}(i)} \right| 100\%}{n} = 2.65\% \tag{2}$$

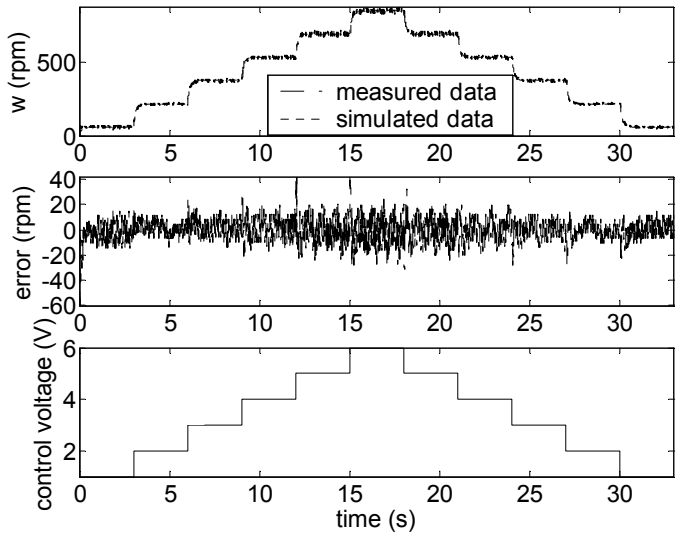

Figure 3: Powder delivery system motor measured and modeled responses to control voltage step signals.

To validate the DC motor model in the frequency domain, sinusoidal voltage signals with different frequencies are sent to the motor amplifier and the resulting motor angular velocities are recorded. The same voltage signals are applied to the model in equation (1). Magnitude and phase information are then extracted from the experimental and simulation data, and the resulting frequency plots are shown in Figure 4. The results show that the model frequency responses match the experimental data very well in the low frequency region.

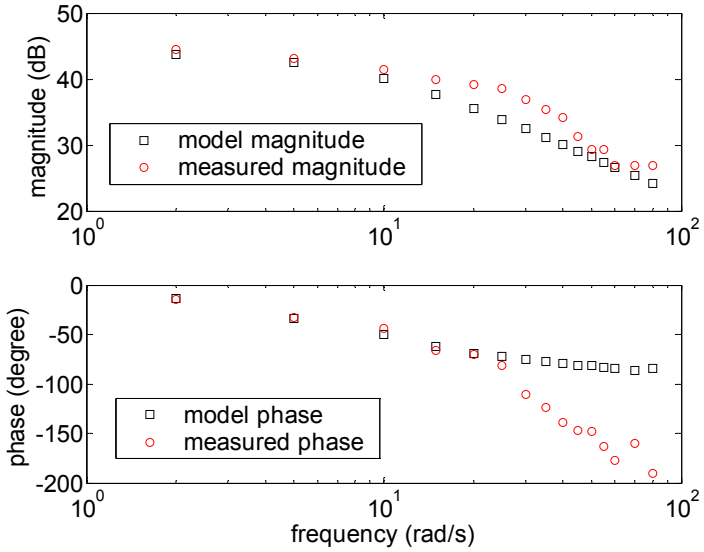

Figure 4: Powder delivery system motor model and experimental rotation speed frequency responses.

3.2 Powder Transport System Model

The powder transport system can be modeled as a first order system with a pure delay due to material transport through the long tubes [9]. The powder transport system dynamic model is

$$\tau_d \dot{p}(t) + p(t) = k_d \omega(t) e^{-T_d} \tag{3}$$

where τ_d is the powder transport system time constant (*sec*), $p(t)$ is the powder flow rate (*gpm*), k_d is the powder transport system steady–state gain (*gpm*/*rpm*), and T_d is the material transport delay (*sec*). To determine the powder delivery system model parameters, an infrared emitter–detector pair is used. It consists of an infrared emitter that produces an infrared beam that is detected by a phototransistor. The emitter–detector pair is installed such that the infrared beam is aimed at the powder focal point. The detector output is an analog voltage that is calibrated to powder flow rate. As the powder flow rate increases, a larger portion of the infrared beam is blocked, resulting in a higher output voltage. This device is installed directly on the nozzle, as shown in Figure 5, and connected to the data acquisition and control system.

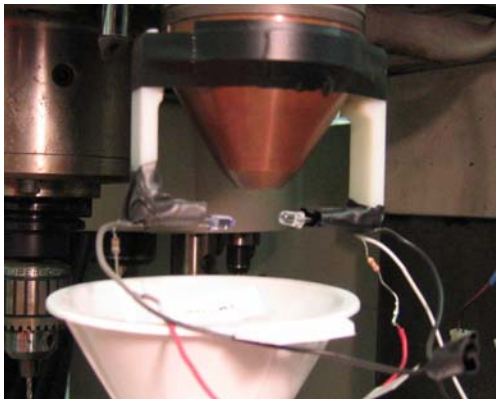

Figure 5: Infrared emitter–detector pair setup used for powder transport system modeling.

In order to determine the powder transport model parameters, a series of step tests are implemented. The results are plotted in Figure 6. The time constant and delay are graphically determined for each step response in Figure 6. The values are averaged and the numerical values are τ_d = 0.601 *sec* and T_d = 0.55 *sec*, respectively. To determine the powder transport system steady–state gain, the Least Squares method is used to determine a linear relationship between the steady–state powder flow rate and the steady–state DC motor rotational speed for the

experiments previously described. This relationship is plotted in Figure 7 and the powder transport system steady–state gain is determined to be 0.082 (*gpm*/*rpm*).

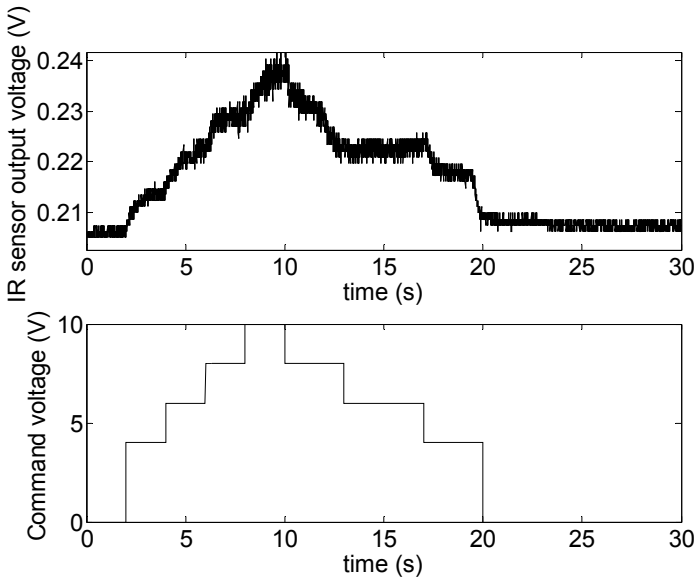

Figure 6: Infrared sensor feedback as a function of powder delivery system command voltages.

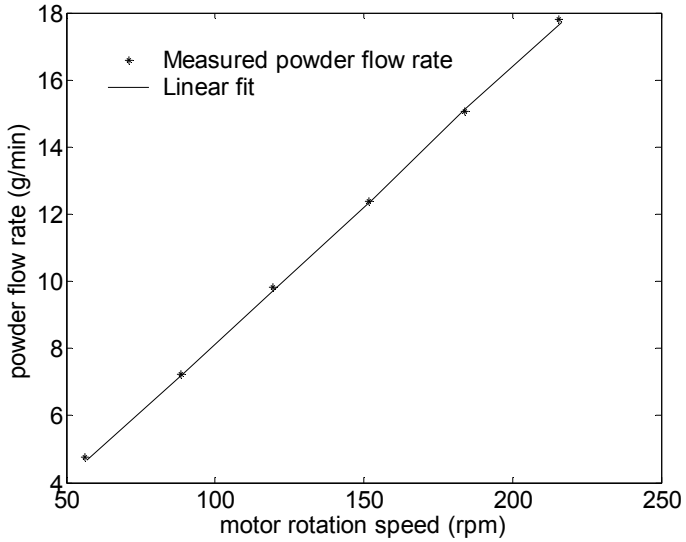

Figure 7: Steady–state powder flow rate versus steady–state motor rotational speed.

3.3 Powder Delivery System Comprehensive Model

The powder delivery system comprehensive model consists of a combination of the DC motor model and the powder transport system model, as illustrated via the block diagram in Figure 8. The control signal is defined as

$$u(t) = V_c(t) - f \tag{4}$$

where $f = \frac{T_f}{k_m}$. Therefore, the powder delivery system comprehensive model is

$$\tau_m \tau_d \ddot{p}(t) + [\tau_m + \tau_d]\dot{p}(t) + p(t) = k_m k_d u(t - T_d) \tag{5}$$

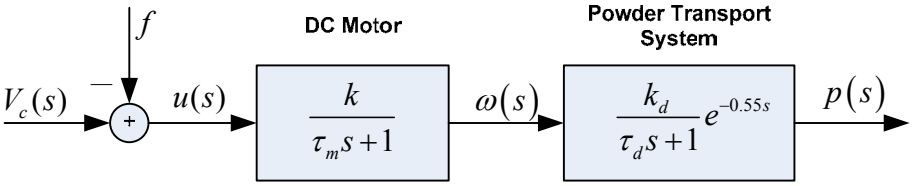

Figure 8: Powder delivery system comprehensive model.

4. Variable Powder Flow Rate Control Methodology

The variable powder flow rate control (VPFRC) methodology includes three parts: feedback controller design, powder flow rate estimation, and powder flow rate reference generation. These parts are described in this section.

4.1 Feedback Controller Design

In order to design a controller that directly regulates the powder flow rate at the nozzle exit, a closed–loop control system, shown in Figure 9, is used. To compensate for the material transport

delay, the reference powder flow rate signal $p_r(t)$ is fed forward by the material transport delay period. The signal $p_1(t)$ is the pseudo powder flow rate produced by the powder delivery system if it did not have a delay, while $p_2(t)$ is the actual powder flow rate at the nozzle.

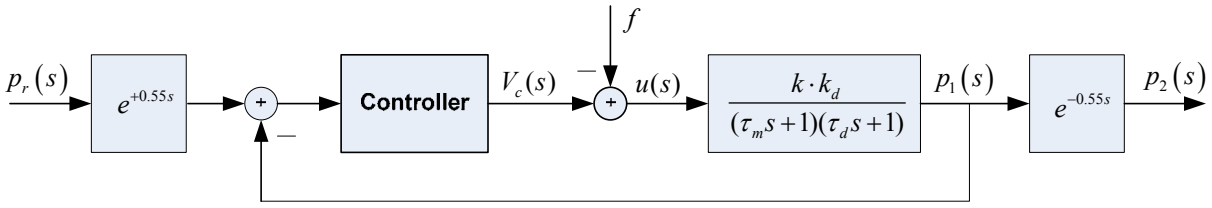

Figure 9: Powder delivery system closed–loop control system block diagram.

The system model used for control design relates the pseudo powder flow rate to the control signal and is

$$\frac{P_1(s)}{U(s)} = \frac{k_m k_d}{\tau_m \tau_d s^2 + (\tau_m + \tau_d)s + 1} = \frac{1}{k_2 s^2 + k_1 s + k_0} \tag{6}$$

where $k_0 = \frac{1}{k_m k_d}$, $k_1 = \frac{\tau_m + \tau_d}{k_m k_d}$, and $k_2 = \frac{\tau_m \tau_d}{k_m k_d}$. The corresponding differential equation is

$$k_2 \ddot{p}_1(t) + k_1 \dot{p}_1(t) + k_0 p_1(t) = u(t) \tag{7}$$

The powder flow rate error is

$$e(t) = p_1(t) - p_{1r}(t) \tag{8}$$

where $p_{1r}(t)$ is the reference pseudo powder flow rate. Combining equations (7) and (8) with the first two derivatives of equation (8)

$$k_2 \ddot{e}(t) + k_1 \dot{e}(t) + k_0 e(t) = u(t) - k_2 \ddot{p}_{1r}(t) - k_1 \dot{p}_{1r}(t) - k_0 p_{1r}(t) \tag{9}$$

The pseudo control signal is

$$\hat{u}(t) = u(t) - k_2 \ddot{p}_{1r}(t) - k_1 \dot{p}_{1r}(t) - k_0 p_{1r}(t) \tag{10}$$

Combining equations (9) and (10)

$$k_2 \ddot{e}(t) + k_1 \dot{e}(t) + k_0 e(t) = \hat{u}(t) \tag{11}$$

The state space form of equation (11) is

$$\begin{bmatrix} \dot{e}_1(t) \\ \dot{e}_2(t) \end{bmatrix} = \begin{bmatrix} 0 & 1 \\ -\dfrac{k_0}{k_2} & -\dfrac{k_1}{k_2} \end{bmatrix} \begin{bmatrix} e_1(t) \\ e_2(t) \end{bmatrix} + \begin{bmatrix} 0 \\ \dfrac{1}{k_2} \end{bmatrix} \hat{u}(t) \tag{12}$$

where $e_1(t) = e(t)$ and $e_2(t) = \dot{e}(t)$. The full state feedback control law is

$$\hat{u}(t) = -G\mathbf{x}(t) \tag{13}$$

where $\mathbf{x}(t) = \begin{bmatrix} e_1(t) & e_2(t) \end{bmatrix}^T$ and G is the controller gain vector determined by the pole placement technique. Theoretically, the controller gain vector can be selected such that the error dynamics are completely specified. In practice, the achievable dynamic response is limited by disturbances and hardware limitations. The control signal is then given by

$$u(t) = k_2 \ddot{p}_{1r}(t) + k_1 \dot{p}_{1r}(t) + k_0 p_{1r}(t) - G\mathbf{x}(t) \tag{14}$$

Combining equations (4) and (14), the physical control signal is

$$V_c(t) = k_2 \ddot{p}_{1r}(t) + k_1 \dot{p}_{1r}(t) + k_0 p_{1r}(t) - G\mathbf{x}(t) + \frac{T_f}{k_m} \tag{15}$$

For implementation, $e(t)$ is measured and $\dot{e}(t)$ is calculated using a first–order backward finite difference scheme. The controller presented here is a general tracking controller that can be applied to any reference trajectory, as opposed to a PID controller that is only guaranteed to track constant powder flow rates.

4.2 Powder Flow Rate Estimation

In the experimental setup, the powder flow rate at the nozzle cannot be directly measured during the deposition process; therefore, it is estimated using a two–step process. First, the DC motor angular speed is estimated with a Kalman filter using the measured motor angular position. Since the powder flow rate is unobservable from the measured motor angular position, the powder flow rate is estimated from the model in equation (3) using the estimated DC motor angular speed as the input. Disturbances (e.g., unmodeled DC motor dynamics, uncertainty in the Coulomb friction value, force ripple) can deteriorate controller performance. To compensate for these disturbances, a Kalman filter is used to estimate a lumped disturbance term and the control signal is modified to directly cancel the estimated disturbance.

The differential equations describing the DC motor motion and disturbance are

$$\begin{aligned} \dot{\theta}(t) &= \omega(t) \\ \dot{\omega}(t) &= -\frac{1}{\tau_m}\omega(t) + \frac{k_m}{\tau_m}\left(u(t) - d(t)\right) \\ \dot{d}(t) &= w(t) \end{aligned} \tag{16}$$

where $\theta(t)$ is the DC motor angular position, $d(t)$ is the disturbance in units of volts, and $w(t)$ is a white noise signal with zero mean and covariance Q_w. The state space form of equation (16) is given by

$$\begin{aligned} \dot{\phi}(t) &= A_E\phi(t) + B_E u(t) + D_E w(t) \\ \varphi(t) &= H_E\phi(t) + \gamma(t) \end{aligned} \tag{17}$$

where $\gamma(t)$ is the measurement noise with covariance R_γ and

$$\phi(t) = \left[\theta(t)\ \omega(t)\ d(t)\right]^T$$
$$A_E = \begin{bmatrix} 0 & 1 & 0 \\ 0 & -\frac{1}{\tau_m} & -\frac{k_m}{\tau_m} \\ 0 & 0 & 0 \end{bmatrix} \tag{18}$$
$$B_E = \begin{bmatrix} 0 & \frac{k_m}{\tau_m} & 0 \end{bmatrix}^T,\ D_E = \begin{bmatrix} 0 & 0 & 1 \end{bmatrix}^T,\ H_E = \begin{bmatrix} 1 & 0 & 0 \end{bmatrix}$$

To apply the Kalman filter, equation (17) is rewritten in discrete form using a zero–order hold

$$\begin{aligned} \phi(k+1) &= A_{Ed}\phi(k) + B_{Ed}u(k) + D_{Ed}w(k) \\ \varphi(k) &= H_{Ed}\phi(k) + \gamma(k) \end{aligned} \tag{19}$$

The Kalman filter algorithm is implemented below. First, the predicted states and error covariance, respectively, are

$$\begin{aligned} \hat{\phi}^p(k+1) &= A_{Ed}\hat{\phi}(k) + B_{Ed}u(k) \\ P^p(k+1) &= A_{Ed}P(k)A_{Ed}^T + D_{Ed}Q_wD_{Ed}^T \end{aligned} \tag{20}$$

where $\hat{\phi}(k)$, $u(k)$, and $P(k)$ are the estimated state, control signal, and error covariance at increment k, respectively. Second, the Kalman gain is

$$K_g(k+1) = P^p(k+1)H_{Ed}^T\left(H_{Ed}P^p(k+1)H_{Ed}^T + R_\gamma\right)^{-1} \tag{21}$$

where $K_g(k+1)$ is the Kalman gain at increment $k+1$. In the last step, the state estimate and error covariance, respectively, are updated with measurement $\varphi(k+1)$

$$\begin{aligned} \hat{\phi}(k+1) &= \hat{\phi}^p(k+1) + K_g(k+1)\left(\varphi(k+1) - H_{Ed}\hat{\phi}^p(k+1)\right) \\ P(k+1) &= \left(I - K_g(k+1)H_{Ed}\right)P^p(k+1) \end{aligned} \tag{22}$$

The covariance matrices Q_w and R_γ are tuned experimentally. Incorporating the disturbance estimate into the control signal in equation (15), the physical control signal that is implemented is

$$\hat{V}_c(k) = k_2 \ddot{p}_{1r}(k) + k_1 \dot{p}_{1r}(k) + k_0 p_{1r}(k) + G\mathbf{x}(k) + \frac{T_f}{k_m} + \hat{d}(k) \tag{23}$$

where $\hat{d}(k)$ is the estimated disturbance at increment *k*. Since the powder flow rate at the nozzle cannot be directly measured, it is estimated by solving the following differential equation

$$\tau_d \dot{\hat{p}}_1(t) + \hat{p}_1(t) = k_d \hat{\omega}(t) \tag{24}$$

where $\hat{\omega}(t)$ is the estimated DC motor angular velocity. A zero–order hold is applied to equation (24) to transform it into the discrete domain. The resulting difference equation is used to compute the estimated powder flow rate on–line.

4.3 Powder Flow Rate Reference Generation

The desired powder distribution along the deposition path is given by

$$\frac{p_r(t) \cdot t}{v(t) \cdot t} = \frac{p_r(t)}{v(t)} = p_d(t) \tag{25}$$

where p_r (*g/min*) is the reference powder flow rate, v (*mm*/*min*) is the motion system velocity along the deposition path, and p_d (*g/mm*) is the desired powder mass distribution per unit length. To maintain a uniform bead morphology, it is necessary for the powder distribution to be constant. To achieve this, the powder flow rate reference is calculated by

$$p_r(t) = v(t)\, p_d \tag{26}$$

In the current experiment setup, the motion system velocity profile is recorded by running the motion program in a "dry run" mode where the powder delivery system and laser are off. This trajectory is used in equation (26) to compute the reference powder flow rate. Since the reference generation scheme used here does not take the deposition dynamics, error in the powder

transport model, etc. into account, the powder flow rate reference trajectory may need to be empirically tuned in order to obtain satisfactory deposition results.

5. Experimental Studies

To evaluate the performance of the variable powder flow rate controller, a series of circular parts are fabricated. The experiment is conducted on three different powder flow rate references: a constant powder flow rate reference, a variable powder flow rate reference based the measured motion system velocity profile, and a modified variable powder flow rate reference based on experimentation. The laser power is maintained at a constant value of 700 W during the entire deposition process. The carrier gas pressure at the powder transport system inlet is maintained at a constant value of 40 kPa. The shielding gas is Argon with a constant gas pressure of 60 kPa. The powder material used in the experiments is H13 tool steel. Each part has a radius of $R = 25.4$ mm, 10 layers, and a commanded velocity along deposition path of $v = 254$ mm/min. The measured velocity along the deposition path is shown in Figure 10. Due to the motion system's interpolation scheme, the velocity is not constant and varies between 230 mm/min and 325 mm/min.

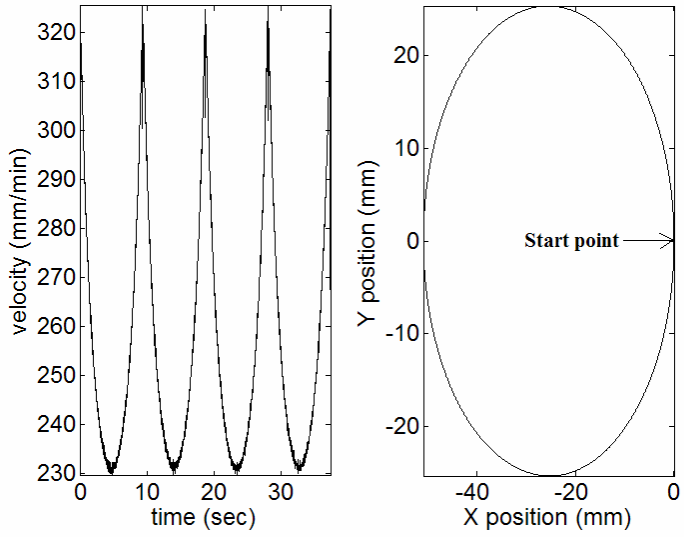

Figure 10: Measured motion system velocity profile for one layer (left) from the execution of a clockwise circle (right, R = 25.4 *mm* and v = 254 *mm/min*).

In the first experiment the original powder delivery system controller is employed with a commanded constant powder flow rate of 8.25 *g/min*. The results are shown in Figure 11. The three–dimensional scan is done with a 3D scanner (Model 2020i from Nextengine) that has a resolution of 0.13 *mm*. Similar to the motion system velocity profile in Figure 10, the part has four sections where the deposition is excessively high and four sections where the deposition is excessively low. The tremendous variation in deposition height is directly due to the variation in the motion system velocity: as the velocity decreases more powder per unit length is deposited and as the velocity increases less powder per unit length is deposited. This corresponds to deposition that is too high and deposition that is too low, respectively.

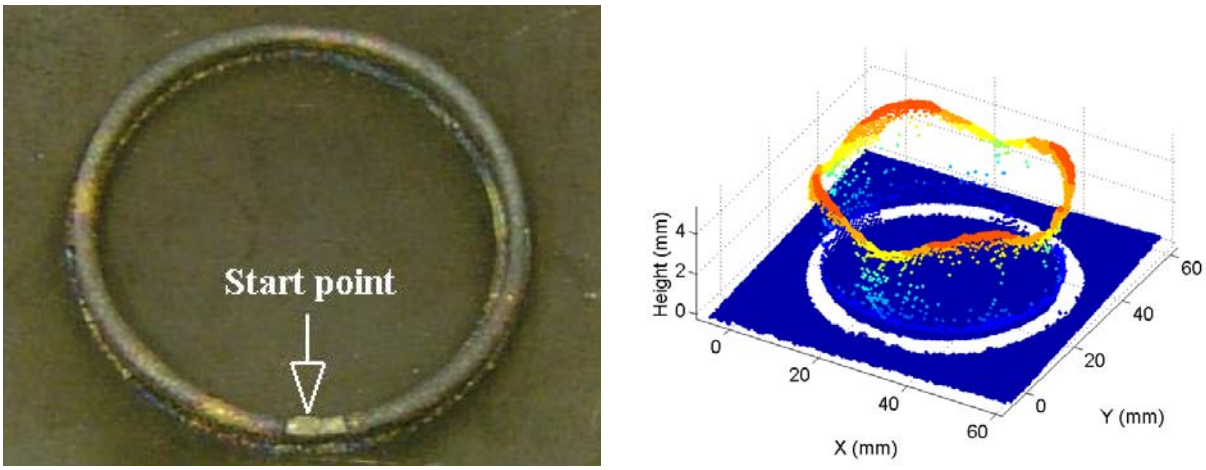

Figure 11: Circular part deposition (left) and three–dimensional scan (right) using constant powder flow rate (p_r = 8.25 *g/min*).

Variable Powder Flow Rate Control is implemented in the next experiment. The powder flow rate reference (shown in Figure 12) is calculated using equation (26) where $v(t)$ is the measured motion system velocity shown in Figure 10 and the desired powder mass distribution per unit length is $3.15 \cdot 10^{-2}$ *g*/*mm*. The reference powder flow rate compensates for the motion system's velocity variation such that a constant powder distribution per unit length is achieved. The results are shown in Figures 13 and 14. The powder flow rate error standard deviation and the absolute value of the maximum powder flow rate error are $8.68 \cdot 10^{-2}$ *g*/*min* and 1.21 *g*/*min*, respectively. The maximum errors occur at the beginning of each layer since the motion system stops when the Z–axis moves upward before the start of a new layer. There is also significant error three other times during each layer when the powder flow rate derivative changes sharply. Although the VPFRC was able to significantly decrease the height variation as compared to the constant powder flow rate controller, part height variations still exist since the laser energy input per unit length changes dramatically as the motion system velocity changes. This, in turn, changes the deposition dynamics, which are not taken into account by varying the powder flow rate.

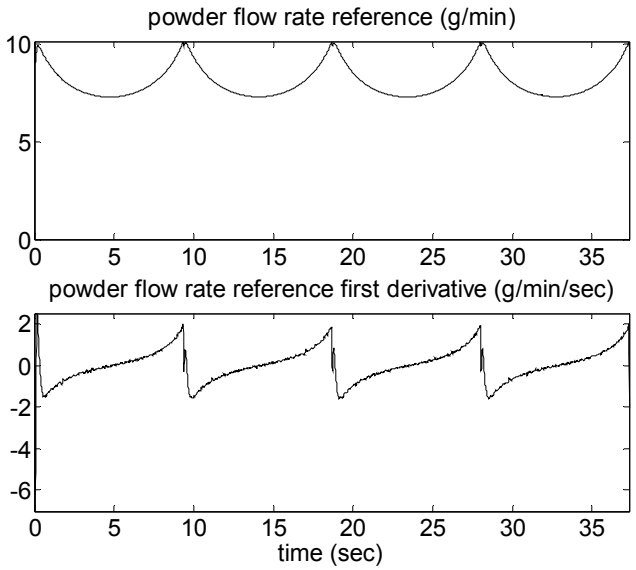

Figure 12: Powder flow reference (top) directly calculated from motion system measured velocity profile and powder flow rate reference first time derivative (bottom).

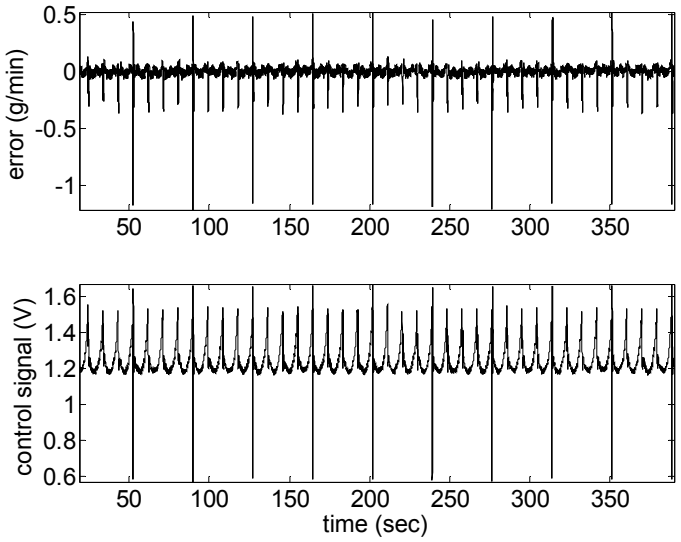

Figure 13: Tracking error and control signal for VPFRC with powder flow rate reference directly computed from motion system velocity.

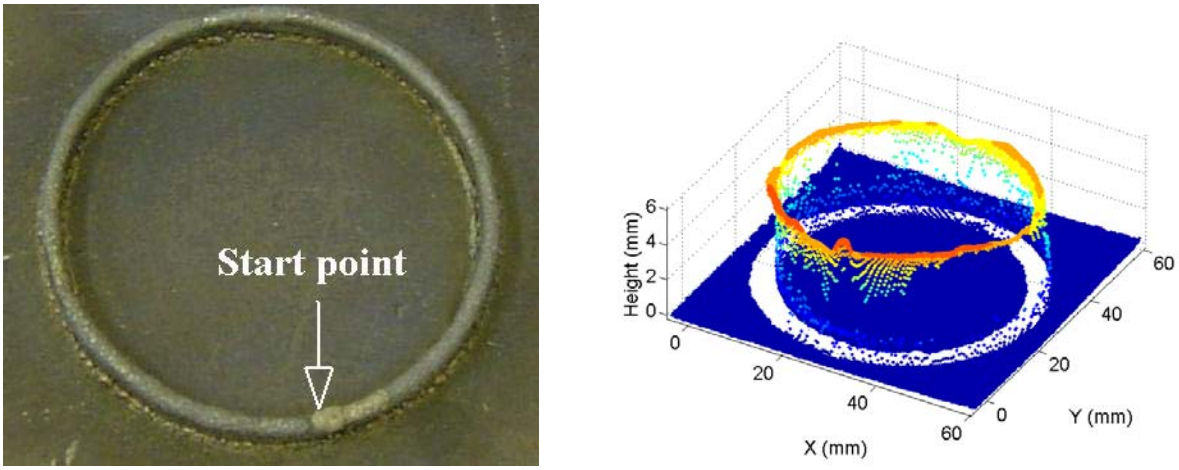

Figure 14: Circular part deposition (left) and scanned three–dimensional result (right) using powder flow rate reference directly computed from motion system velocity.

If a process model were available that related both the laser energy input and powder flow rate to the part height, this model could be utilized to generate the appropriate powder flow rate reference trajectory. Since such a model is not currently available, the powder flow rate reference trajectory was manually adjusted to account for the change in laser energy input as the motion system velocity varied. The modified powder flow rate reference is shown in Figure 15. The controller tracking results are presented in Figures 16 and 17. The powder flow rate error standard deviation and the absolute value of the maximum powder flow rate error are $5.27 \cdot 10^{-2}$ *g*/*min* and 0.284 *g*/*min*, respectively. The error spikes again occur when the Z–axis moves upward before the start of a new layer and when the powder flow rate derivative changes sharply. However, these errors have decreased due to the fact that the powder flow rate trajectory is smoother (i.e., the derivative changes are not as sharp). The VPFRC with a modified powder flow rate reference was able to significantly decrease the part height variation as compared to the

constant powder flow rate controller and the VPFRC with an unmodified powder flow rate reference.

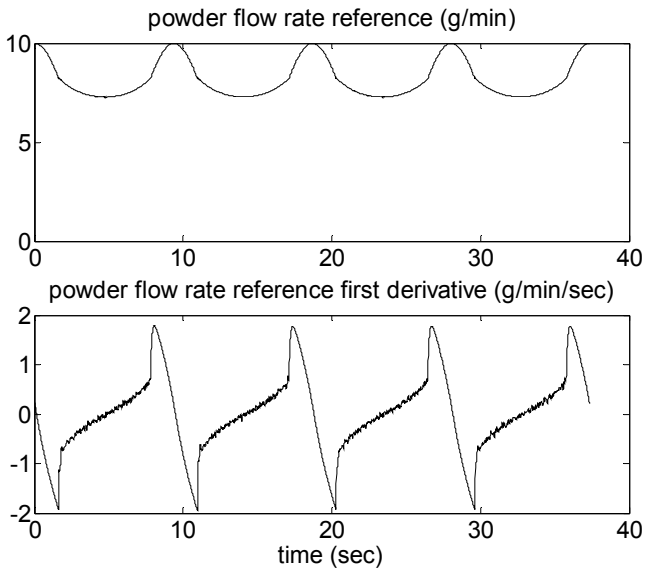

Figure 15: Modified powder flow reference (top) determined experimentally and powder flow rate reference first time derivative (bottom).

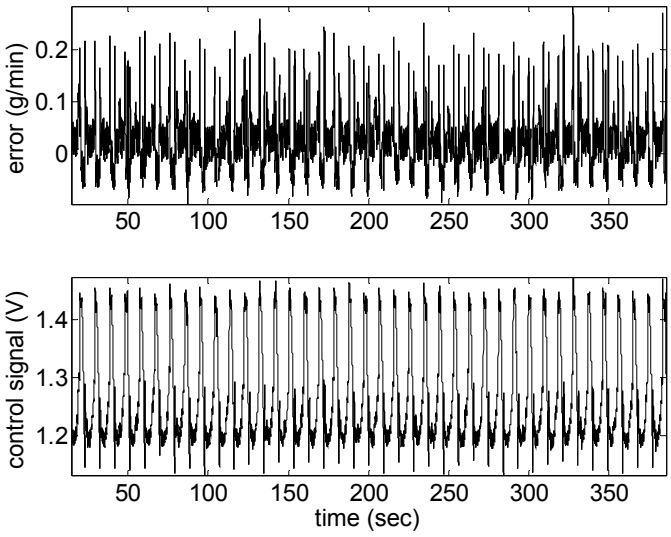

Figure 16: Tracking error and control signal for VPFRC with modified powder flow rate reference determined experimentally.

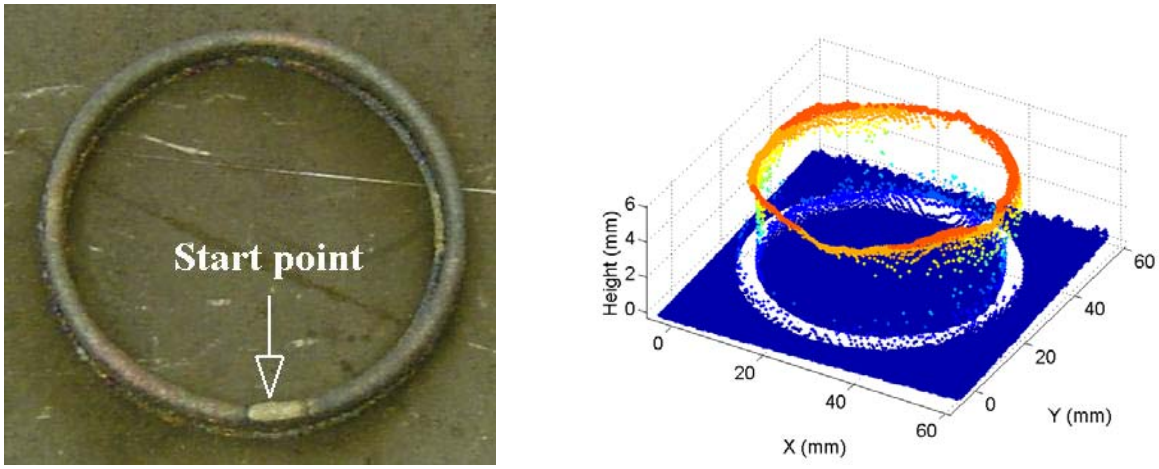

Figure 17: Circular part deposition (left) and three–dimensional scan (right) using modified powder flow rate reference determined experimentally.

The height of the parts shown in Figures 11, 14, and 17 where each measured at sixteen equally spaced locations using a caliper. The results are shown in Figure 18. The minimum, mean,

maximum, peak to peak, and standard deviation of the part heights is given in Table 1. The decrease in peak to peak and standard deviation were 13% and 27%, respectively, for the part fabricated with the VPFRC (directly calculated reference) as compared to the part fabricated with a constant powder flow rate. The decrease in peak to peak and standard deviation were 43% and 43%, respectively, for the part fabricated with the VPFRC (modified reference) as compared to the part fabricated with a constant powder flow rate. These results illustrate the ability of the VPRFC methodology to decrease variable in the part geometry.

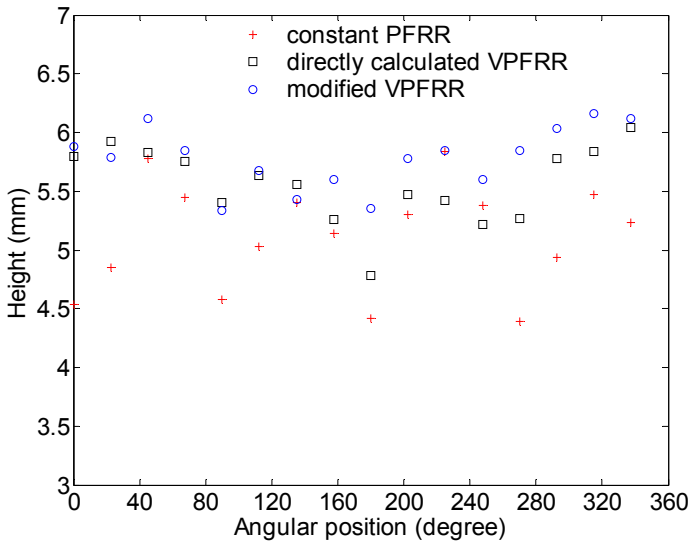

Figure 18: Deposition results comparison between constant and variable powder flow rate reference (VPFRR)

Table 1: Controller Comparison in Regards to Part Height.

Controller	Maximum Height (*mm*)	Mean Height (*mm*)	Minimum Height (*mm*)	Peak to Peak Height (*mm*)	Standard Deviation (mm)
Constant Powder Flow Rate Controller	5.84	5.11	4.39	1.45	0.44
VPFRC (direct reference)	6.04	5.56	4.78	1.26	0.32
VPFRC (modified reference)	6.16	5.78	5.34	0.82	0.25

6. Summary and Conclusions

A powder flow rate control methodology called Variable Powder Flow Rate Control (VPFRC) was proposed in this paper. This methodology utilizes a non–constant reference powder flow rate trajectory to account for changes in the motion system velocity along the deposition path, thereby maintaining a constant powder deposition per unit length for a more uniform track morphology. The VPFRC methodology includes a controller capable of tracking general reference powder flow rate trajectories, a measurement–model based powder flow rate estimator, and a powder flow rate reference trajectory generation scheme. Three circular parts were deposited and analyzed to evaluate the controller performance. These three parts were deposited using three different powder flow rate references: constant reference, variable reference directly calculated from the measured motion system velocity profile, and a modified variable reference determined experimentally.

The experimental results demonstrate that the VPFRC methodology is able to robustly track the powder flow rate references, even though these references are not constant. The fabrication of the circular parts demonstrated that using a variable reference powder flow rate substantially decreases part height variation, as compared to a constant powder flow rate. In the experiments conducted in this paper the laser power was constant. Therefore, the dilution varied significantly when a constant powder distribution per unit length was supplied and the motion system velocity varied. A modified reference powder flow rate was utilized to account for this issue. The experimental results demonstrated that the part height variation was reduced substantially as compared to the part fabricated with the unmodified reference powder flow rate. To achieve

maximum part quality, the laser power and powder mass flow rate must be coordinated. Therefore, the integration of the laser power and powder mass flow rate control will be considered in future studies.

Acknowledgement

The authors gratefully acknowledge the financial support of the Intelligent Systems Center at the University of Missouri–Rolla.

References

[1] Choi, J., 2002, "Process and Prosperities Control in Laser Aided Direct Metal/Materials Deposition Process," *Proceedings of IMECE*, New Orleans, Louisiana, November 17–22, pp. 1–9.

[2] Griffith, M.L., Keicher, D.M., Atwood, C.L., Romero, J.A., Smegeresky, J.E., Harwell, L.D., and Greene, D.L., 1996, "Free Form Fabrication of Metallic Components Using Laser Engineered Net Shaping (LENS)," *Solid Freeform Fabrication Symposium*, Austin, Texas, August 12–14, pp. 125–131.

[3] Hu D., Mei H., and Kovacevic, R., 2001, "Closed Loop Control of 3D Laser Cladding Based on Infrared Sensing," *Solid Freeform Fabrication Symposium*, Austin, Texas, August 6–8, pp. 129–137.

[4] Hu, Y.P., Chen, C.W., and Mukherjee, K., 1997, "An Analysis of Powder Feeding Systems on the Quality of Laser Cladding," *Advances in Powder Metallurgy and Particulate Materials*, Vol. 3, Chicago, Illinois, June 29–July 2, pp. 21.17–21.31.

[5] Hu, D. and Kovacevic, R., 2003, "Sensing, Modeling and Control for Laser–Based Additive Manufacturing," *International Journal of Machine Tools and Manufacture*, Vol. 43, No. 1, pp. 51–60.

[6] Li, L. and Steen, W.M., 1993, "Sensing, Modeling and Closed Loop Control of Powder Feeder for Laser Surface Modification," *ICALEO*, pp. 965–975.

[7] Thayalan, V. and Landers, R.G., 2006, "Regulation of Powder Mass Flow Rate in Gravity–Fed Powder Feeder Systems," *SME Journal of Manufacturing Processes*, Vol. 8, No. 2, pp. 121–132.

[8] Kennedy J. and Eberhart R.C., 1995, "Particle Swarm Optimization," *IEEE International Conference on Neural Networks*, Perth, Australia, November 27–December 1, pp. 1942–1948.

[9] Landers, R.G., Pan, H., and Liou, F.W, 2006, "Dynamic Modeling of Powder Delivery Systems in Gravity–Fed Powder Feeders," *ASME Journal of Manufacturing Science and Engineering*, Vol. 128, No. 1, pp. 337–345.